Lee et al. *NPG Asia Materials* (2020) 12:28
https://doi.org/10.1038/s41427-020-0204-0

NPG Asia Materials

ARTICLE Open Access

# Binder- and conductive additive-free laser-induced graphene/$LiNi_{1/3}Mn_{1/3}Co_{1/3}O_2$ for advanced hybrid supercapacitors

Seung-Hwan Lee[1,2], Ki-Yong Kim[1] and Jung-Rag Yoon[3]

**Abstract**

Hybrid supercapacitors have recently emerged as next-generation energy storage devices that bridge the gap between supercapacitors and lithium-ion batteries. However, developing high energy cathodes that maintain long-term cycle stability and a high rate capability for real applications remains a significantly challenging issue. Herein, we report a facile synthesis method for a laser-scribed graphene/$LiNi_{1/3}Mn_{1/3}Co_{1/3}O_2$ (LSG/NMC) composite for high energy cathode materials for use in hybrid supercapacitors. LSG/NMC composites exhibit not only a high capacitance of up to 141.5 F/g but also an excellent capacitance retention of 98.1% after 1000 cycles at a high current density of 5.0 A/g. The introduction of an NMC spacer between the LSG layers provides an enlarged interspace that can act as an efficient channel for additional storage sites and rapid access. In addition, we further confirmed that hybrid supercapacitors using LSG/NMC cathodes and $H_2T_{12}O_{25}$ anodes with an $AlPO_4$/carbon hybrid coating layer (H-HTO) deliver a remarkable energy density of ~123.5 Wh/kg, power density of ~14074.8 W/kg, and a long-term cycle stability of 94.6% after 20,000 cycles. This work demonstrates that our proposed material can be considered a strong cathode candidate for next-generation hybrid supercapacitors.

## Introduction

Currently, many researchers are studying high-performance energy storage devices (ESDs) as alternative energy sources to replace fossil fuels[1,2]. Among them, lithium-ion batteries (LIBs) are the most widely used ESDs so far. Although LIBs have an excellent energy density (130–200 Wh/kg), they also have a low power density (below 1 kW/kg) and short life expectancy[3,4]. In contrast, supercapacitors, also known as electrical double-layer capacitors, can facilitate fast charge transport, owing to their excellent power density (<15 kW/kg). The opinion that the future of electric vehicles (EVs) depend on supercapacitors rather than LIBs was suggested by Elon Musk in 2011[5]. However, supercapacitors have also suffered from a low energy density (<10 Wh/kg) in practical applications, as summarized in Table 1[6]. This is because supercapacitors consist of symmetrical electrodes made of activated carbon (AC), which has a low capacity of ~30 mAh/g[7].

Recently, hybrid supercapacitors, having the advantages of both supercapacitors and LIBs, have been studied as novel ESDs that can deliver a long cycle life, high energy density, and power density[7]. Hybrid supercapacitors comprise a hybrid system that contains a battery-like transition-metal oxide anode and a capacitor-like AC cathode[8]. The charge storage mechanism of hybrid supercapacitors is a combination of anion adsorption/desorption (a physical reaction) and Li-ion intercalation/deintercalation (a chemical reaction). On the other hand, Li-ion capacitors that comprise prelithiated (i.e., predoped with Li ions) graphite and AC deliver a high energy density and have been highlighted as promising candidates for future ESDs. However, they have an electrochemical

Correspondence: Seung-Hwan Lee (shlee83@umd.edu) or Ki-Yong Kim (kykim@umd.edu)
[1]Institute for Research in Electronics and Applied Physics, University of Maryland, College Park, MD 20742, USA
[2]Department of Advanced Materials Engineering, Daejeon University, Daejeon 34520, Republic of Korea
Full list of author information is available at the end of the article.

**Table 1 Comparison of the performance of supercapacitors, hybrid supercapacitors, LICs, and Li-ion batteries.**

| Energy Storage Device | Supercapacitors | Hybrid supercapacitors | Li-ion capacitors | Li-ion batteries |
|---|---|---|---|---|
| | 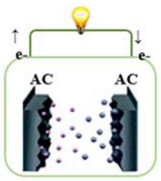 | 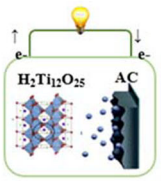 | 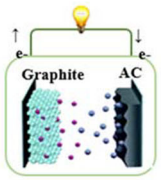 | 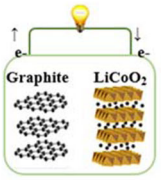 |
| Charge storage mechanism | Physical reaction | Physical & Chemical reaction | Physical & Chemical reaction | Chemical reaction |
| Advantage | High P/D | Improved E/D with similar P/D | High E/D | High E/D |
| Disadvantage | Low E/D | Still low E/D | Unsafety issue and costly manufacturing | Low P/D |
| E/D | <10 Wh/kg | 3 ~ 68 Wh/kg | 7 ~ 70 Wh/kg | 130 ~ 200 Wh/kg |
| P/D | 0.5 ~ 15 kW/kg | 1 ~ 10 kW/kg | 0.8 ~ 11 kW/kg | <1 kW/kg |

performance that is one-third that of hybrid supercapacitors under subzero temperatures, high manufacturing costs, and safety problems, which are substantial obstacles for commercialization[9–13]. Hybrid supercapacitors can deliver much more energy than supercapacitors without sacrificing the power density through a novel approach, which can be explained by the use of new electrode materials that increase the operating voltage window, as shown in Fig. 1[13]. In addition, battery-type anodes deliver a capacitance that is several times higher than that of an AC anode (30 mAh/g). There are currently three research directions for high-performance hybrid supercapacitors[14]. The first is to improve the power density and lifetime of the battery-type anode. The second is to achieve high safety and reliability through suppression of the swelling phenomenon. The third is to increase the energy density of the supercapacitor-type cathode[15–18]. Among them, the research to improve the energy density of hybrid supercapacitors is addressing the most important issue. The total capacity ($C_T$) of hybrid supercapacitors can be derived from the following equation[19]:

$$\frac{1}{C_T} = \frac{1}{C_a} + \frac{1}{C_c} \quad (1)$$

where $C_a$ is the anode capacity and $C_c$ is the cathode capacity. In the case of hybrid supercapacitors, both capacities for the two electrodes are different. Supplementary Table S1 compares the $C_T$ for supercapacitors and hybrid supercapacitors. For hybrid supercapacitors, we added two cases that consider the following: (1) an anode capacity increase and (2) a cathode capacity

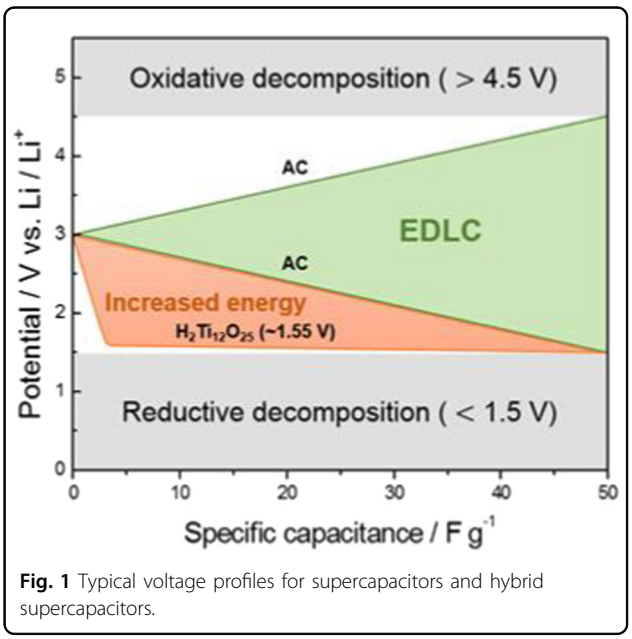


**Fig. 1** Typical voltage profiles for supercapacitors and hybrid supercapacitors.

increase. As a result, we can confirm that increasing the $C_c$ value (which is much lower than the $C_a$ value) is a very effective strategy for obtaining an increased $C_T$ for hybrid supercapacitors.

It is well known that the real capacitance of carbon-based electrodes that are used as cathodes in hybrid supercapacitors is mainly affected by the effective surface area and pore structure. To date, AC has been widely used as a cathode in commercial devices due to its high surface area (1000–2000 $m^2$/g), relatively good capacitance (~120 F/g), and cost effectiveness[2,20]. However, an

unwanted capacitance loss (~10–20%) occurs; the loss is due to the ineffective wetting of the electrolyte on the AC surface via micropore blockage and/or the inability to successfully form a double layer in the pores[21]. Many studies on graphene production methods have been reported, because graphene has been applied to energy storage as an alternative to AC due to its wide specific surface area (2630 $m^2$/g), excellent capacitance (~550 F/g), high electrical conductivity (~$1 \times 10^3$ S/cm), and good mechanical strength (42 N/m)[22–25]. Among the various manufacturing methods, the laser scribing method can be regarded as a promising breakthrough, as an effective and simple strategy for graphene fabrication. The oxygen-containing group GO is effectively removed via deoxygenation and exfoliation simultaneously without a reducing agent[26]. As-prepared LSG can be used as an electrode immediately without binders and conductive additives. Importantly, LSG can also prevent uncontrollable graphene aggregation, because there is no additional electrode-manufacturing process. Therefore, we conclude that laser scribing is the most effective way to obtain high-performance graphene with cost-effective and single-step approach that enables fast production[27,28].

To effectively reduce the stacking and agglomeration of graphene during the reduction process, the incorporation of various transition-metal oxides as spacers between the graphene layers has been studied[29–31]. This method allows for excellent electrochemical performance due to the synergistic combination of the spacer and pseudocapacitive behaviors from the transition-metal oxides. Among various spacer materials, $LiNi_{1/3}Mn_{1/3}Co_{1/3}O_2$ (NMC) has emerged as a promising candidate due to its high energy density ($LiCoO_2$), high thermal stability ($LiMn_2O_4$), and high reversible capacity ($LiNiO_2$), which are the key factors that determine the performance of ESDs[29]. We noted that high-performance hybrid supercapacitors should have more than twice the energy density of supercapacitors without sacrificing the power density and cyclability; this can be accomplished by the addition of a small amount of NMC on the LSG surface. However, an excessive amount of NMC is not helpful for actual applications due to the degradation of the long-term cyclability and power density. Consequently, we adopted an LSG/NMC composite as a promising cathode candidate to improve the $C_T$ of hybrid supercapacitors and this is the first attempt to apply LSG/NMC to hybrid supercapacitors.

Among the various anode materials, $H_2T_{12}O_{25}$ (HTO) exhibited a high initial discharge of 229 mAh/g with a high power density and stable cycle performance. HTO has an unusual tunnel structure, providing additional space for the storage of Li ions and resulting in excellent kinetics[11]. Moreover, the surface of the HTO was modified by a hybrid coating layer having excellent ionic and electronic conductivity, as well as stability. This is because hybrid coatings composed of two channels not only move Li ions ($AlPO_4$) and electrons (carbon) efficiently but also suppress swelling, as shown in Supplementary Fig. S1a[30].

In this study, we report a simple and effective approach to synthesize LSG/NMC composites as a high-capacitance cathode for advanced hybrid supercapacitors. Moreover, we demonstrate the extraordinary electrochemical performance of LSG/NMC composite compared with that of AC and LSG electrodes. The NMC spacer between the LSGs not only keeps the neighboring LSGs separated and provides abundant spaces but also acts as a pseudocapacitive active material, which improves the electrochemical performance. We also use HTO as a high-power anode after applying a surface modification with $AlPO_4$ and carbon hybrid coating (H-HTO). This novel design accelerates the movement of Li ions and electrons, and suppresses the side reaction at the H-HTO/electrolyte interface.

Finally, we studied the electrochemical performance of hybrid supercapacitors using an LSG/NMC cathode and an H-HTO anode (LSG/NMC//H-HTO) to evaluate their practical application. This novel system delivers excellent performance and outperforms previously reported hybrid supercapacitors in terms of the energy and power densities. This can be explained by the combination of the high-capacitance LSG/NMC cathode and fast Li-ion storage and cyclic stability of the H-HTO anode. These findings offer a new perspective for high-performance hybrid supercapacitors.

## Experimental section

To prepare NMC, acetate ($Ni(Ac)_2{\cdot}4H_2O$, Aldrich, USA), cobalt acetate ($Co(Ac)_2{\cdot}4H_2O$, Aldrich, USA), and manganese acetate ($Mn(Ac)_2{\cdot}4H_2O$, Aldrich, USA) were mixed at a molar ratio of Ni : Co : Mn = 1 : 1 : 1. Afterward, lithium acetate ($LiAc{\cdot}2H_2O$, Aldrich, USA) was added to the mixture at a molar ratio of 2.1 : 1 : 1 : 1 (excess Li sources were added to compensate for Li volatilization inhibition during heat treatment). The mixture was heat treated at 500 °C for 4 h and 850 °C for 8 h. Then, the as-synthesized NMC powders were mixed with GO in aqueous solution. The mixture was dispersed by ultrasonication for 180 min and then the homogeneous solution was dropped directly onto an aluminum foil, which was glued to a DVD disk for laser treatment. After drying under ambient conditions for 24 h, the dried film was inserted into a DVD burner (Hitachi/LG GH40L, 788 nm laser with a 5 mW maximum power) for 5 h, to prepare the LSG/NMC composite. The LSG/NMC composite can be used directly as a cathode for hybrid supercapacitors without the addition of a binder and conductive additives, as shown in Fig. 2. The mass ratio of the LSG to NMC was 95 : 5. An AC electrode was fabricated by mixing AC (90 wt%, Samwha Capacitor Co., Ltd) with carbon black (Super P, 5 wt%) and polytetrafluoroethylene (5 wt%).

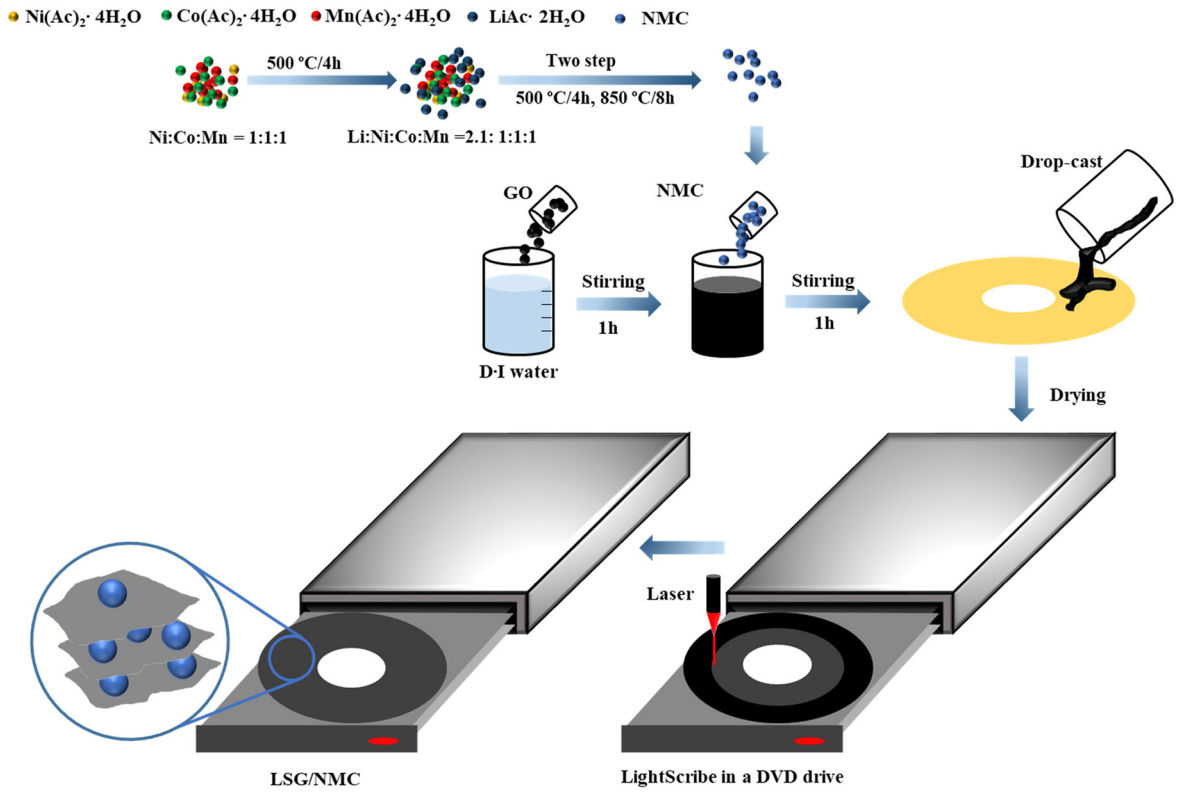


**Fig. 2 Schematic illustration of the LSG/NMC preparation procedure.** The as-synthesized NMC and GO were first suspended in deionized (DI) water. Then, the solution was dropped onto aluminum foil that was glued to the surface of a DVD disk. The NMC/GO-coated DVD disk was then inserted into a DVD optical drive for laser treatment.

To produce H-HTO, $Na_2Ti_3O_7$ precursor was prepared by a conventional solid-state reaction using $Na_2CO_3$ and $TiO_2$ at a molar ratio of 1:3. This mixture was heated at 800 °C for 20 h in air. $H_2Ti_3O_7$ was prepared from the resultant $Na_2Ti_3O_7$ via a $Na^+/H^+$ ion exchange reaction using a 1 M HCl solution for 3 days at 60 °C. The prepared $H_2Ti_3O_7$ was washed with deionized water until the pH was equal to 7 and then dried at 100 °C for 24 h. Finally, HTO was obtained by heating the $H_2Ti_3O_7$ sample at 300 °C for 5 h. The as-prepared HTO powder was mixed with the Super P carbon black used as a carbon source and polyvinylidene fluoride (PVDF) with a weight ratio of 83 : 7 : 10 in distilled water and then ball milled for 3 h. This solution was added to gelatin (an amphoteric surfactant) solution by dissolving gelation in distilled water at 50 °C for 2 h. $Al(NO_3)_3{\cdot}9H_2O$ (0.3 g) and $(NH_4)_2HPO_4$ (0.1 g) were added to distilled water to prepare an $AlPO_4$ suspension (comprising $AlPO_4$ nanoparticles). Subsequently, the HTO powder that was mixed with carbon were added to the $AlPO_4$ suspension and mixed until the final viscosity of the slurry reached ~100 P. The $AlPO_4$ suspension and HTO powder that was mixed with carbon were mixed at a mass ratio of 5 : 95. The mixture was dried at 100 °C for 24 h and finally annealed at 300 °C for 3 h. The synthesis process of H-HTO is illustrated in Supplementary Fig. S1b. For the anode, the H-HTO was mixed with the conductive carbon black binder (Super P) and PVDF (at a weight ratio of 83 : 7 : 10), and then *N*-methyl pyrrolidinone (NMP) solvent was added. The mixed slurry was cast on aluminum foil to a thickness of 70–150 μm via a bar coater and then dried at 100 °C to evaporate the NMP solvent. After that, the aluminum foil was pressed to a thickness of 40–90 μm.

For the half-cell test, the electrodes were prepared with a Li metal counter electrode based on Celgard separators. The hybrid supercapacitors were fabricated in the form of an assembled 2016-type coin cell inside an argon-filled glove box. Afterwards, the jelly roll was dried in a vacuum oven for 48 h to remove moisture and then impregnated with a 1.5 M $LiPF_6$ solution in 1:1 ethylene carbonate : dimethyl carbonate as the electrolyte. Finally, the LSG/NMC cathode, H-HTO anode, and separator were assembled inside an argon-filled glove box. The structural properties were analyzed using X-ray diffraction (XRD), transmission electron microscopy (TEM), scanning TEM (STEM) with energy-dispersive X-ray spectrometry (EDS), X-ray photoelectron spectroscopy (XPS), and Raman spectroscopy. The surface areas of the LSG/NMC and

LSG samples were measured with a Quantachrome Autosorb-3b Brunauer–Emmett–Teller (BET) surface analyzer. The galvanostatic charge–discharge curves, rate capabilities, and cycle performances were measured using an Arbin BT 2042 battery test system at various current densities. The cyclic voltammograms (CVs) were measured using a potentiostat (IviumStat) and electrochemical impedance spectroscopy (EIS) was conducted using a CHI660D electrochemical workstation in the frequency range of $10^{-1}$ to $10^{5}$ Hz.

## Results and discussion

The LSG/NMC composite was easily synthesized with the facile reduction process that was described in the Experimental Section. The XRD patterns in Fig. 3a show that the LSG contains LSG ($2\theta = 26.44°$) and GO ($2\theta = 10.75°$) diffraction peaks, which is different from the XRD pattern for the GO ($2\theta = 10.75°$), which contains only one diffraction peak (Supplementary Fig. S2a). The presence of a GO peak in the LSG can be explained by the fact that only the upper part of the LSG is reduced and the lower part is maintained as GO[31]. However, the intensity of the GO peak in the LSG decreases, indicating that additional GO could be reduced to LSG. Moreover, the GO peak is no longer observed in the LSG/NMC diffraction pattern. This is because the GO is completely reduced as a result of the addition of the NMC spacer. The other additional diffraction peaks are attributed to crystalline NMC (hexagonal α-$NaFeO_2$ with the structure space group: *R3m*)[32]. The XRD patterns of H-HTO are well indexed with those of HTO with a space group *P2/m* and there are no other impurity phases after the surface modification and heat treatment, as shown in Fig. 3b[5]. These results are due to a very low content of $AlPO_4$ and carbon that exceeds the instrument detection limit[33].

The formation of LSG/NMC composite was further confirmed by Raman spectroscopy, which has played an important role in investigating the structural characterization of graphite-based materials. The main peaks in the Raman spectra for the LSG/NMC, LSG, and GO are

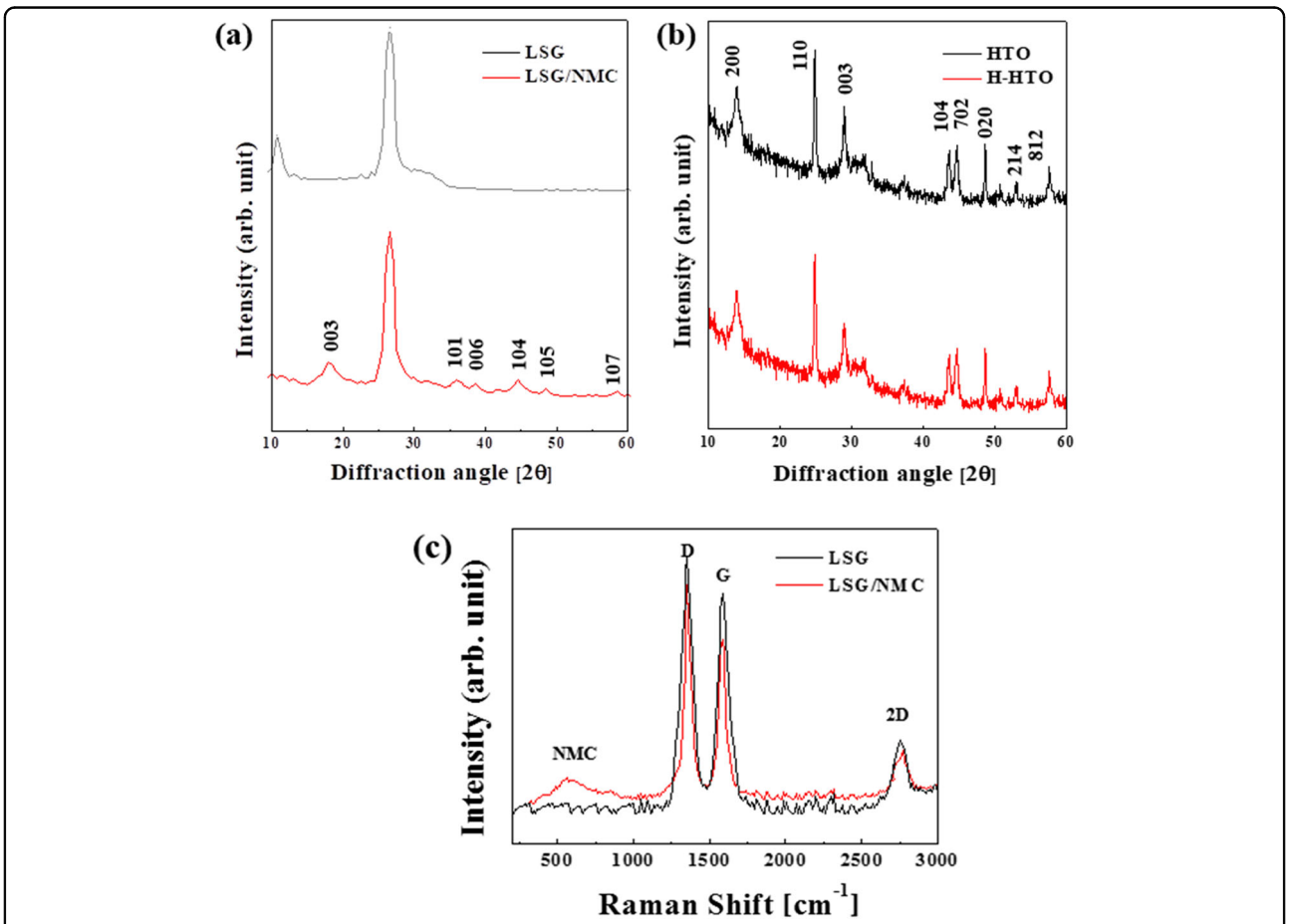


**Fig. 3 Structural characterization of H-HTO, LSG, and LSG/NMC.** XRD patterns of (**a**) LSG/NMC composite and LSG. The diffraction peak ($2\theta = 26.44°$) indicates that the GO was reduced to LSG. Other diffraction peaks were attributed to the NMC. **b** XRD pattern of the H-HTO. **c** Raman spectra of the LSG/NMC composite and LSG. There is a D peak at per 1355 $cm^{-1}$, G peak at 1586 $cm^{-1}$, and 2D peak at 2755 $cm^{-1}$ for the LSG/NMC composite.

from the G-band, D-band, and second-order D-band (2D band), as shown in Fig. 3c and Supplementary Fig. S2b. All Raman bands had changes in their peak shape, position, and intensity, indicating tuning of the structural and electronic properties[34]. The LSG/NMC, LSG, and GO exhibit a couple of Raman-active G bands (in-plane vibration of $sp^2$-bonded carbon atoms) and D bands ($sp^3$ defects or disorder in carbon). However, the LSG/NMC and LSG samples have a sharp and single 2D band, strongly indicating the conversion from GO to graphene[35]. Intense Raman bands can be observed at 1345 and 1605 $cm^{-1}$, corresponding to the well-documented D and G bands for GO, respectively. The Raman features in the LSG spectrum also contain D bands at 1355 $cm^{-1}$ and G bands at 1586 $cm^{-1}$. Compared with that for the GO, the D-band position slightly changed due to larger structural edge defects and smaller graphene domains. The width of the D-band for the LSG slightly decreases but does not change significantly. GO is a carbon lattice that contains oxygen functional groups, which break carbon–carbon bonds to form a strong D-band. The carbon–oxygen bond of GO is broken and oxygen is released during laser treatment. C–C recombination is difficult, as there is a thickness expansion due to the laser treatment and the LSG transforms into loosely stacked films[31,36]. The narrowing G-band also shifts from 1605 to 1586 $cm^{-1}$ via reduction of the oxygen functional group[37]. Notably, the LSG/NMC composite has Raman peaks from both weakened LSG and NMC, indicating a hybrid material composed of LSG and NMC. The Raman peak located at 585 $cm^{-1}$ is attributed to the M–O symmetrical stretching vibration from the Raman modes of $A_{1g}$ in NMC, which is consistent with a previous report[38]. The intensity ratio of the D and G bands ($I_D/I_G$) is well known to assess the disorder of graphene. There is no significant difference between the D-band and the G-band intensity after laser scribing. The $I_D/I_G$ of LSG/NMC sample is smaller than that from the LSG sample due to a reduction in the average size of the $sp^2$ domains of the carbon atoms as a result of the crystallization process of NMC. This means that the NMC spacer created LSG with abundant interstitial spaces, which is favorable for ion storage and electron kinetics, resulting in not only numerous active sites but also excellent electrochemical performance. Contrary to that for the GO, the LSG/NMC and LSG samples have an intense 2D band, the most prominent feature for graphene. The shape and intensity of the 2D band are related to the number of graphene layers. The high 2D band of LSG ($I_{2D}/I_G$ ratio of ~0.36, FWHM of 66 $cm^{-1}$) is observed at an increased frequency of ~2755 $cm^{-1}$, similar to previously reported values for trilayer graphene[39,40]. The LSG/NMC sample exhibits higher $I_{2D}/I_G$ ratio of 0.41 compared with that for the LSG sample (0.38). This outcome could be explained by the contribution of the NMC spacer. From the Raman analysis, we can infer that successful LSG/NMC and LSG materials were prepared with the laser scribing method.

Supplementary Fig. S2c, d shows the $N_2$ adsorption–desorption isotherms of the LSG/NMC and LSG samples. The BET measurement shows that the LSG/NMC composite has a specific surface area of 687.5 $m^2/g$ with a conductivity of 1758 S/m, which is higher than that for the LSG that had a specific surface area of 573.6 $m^2/g$ with a conductivity of 1529 S/m. A hysteresis loop in the $N_2$ adsorption/desorption isotherms from the LSG/NMC and LSG samples is also observed, indicating that both have porous structures. However, the LSG/NMC composite possesses a larger surface area for the LSG because of the NMC spacer between LSG layers. The NMC helps to disperse the LSG and prevent agglomeration of the LSG. The surface area and pore size are directly related to the high capacitance that is achieved for the carbon-based electrodes; this characteristic is associated with a large ion-accessible surface area at the interface between the electrode and electrolyte, ensuring excellent electrochemical performance. The pore-size distributions for the LSG and LSG/NMC samples were obtained by means of the Barrett–Joyner–Halenda model, as shown in the insets of Supplementary Fig. S2c, d, respectively. The hierarchical pore distribution can be confirmed in both electrodes. The LSG/NMC composite shows more mesopores and macropores than that of the LSG. This can be explained by the separation of the LSG by the NMC spacers. This encourages electrical double-layer formation and improves the ion accessibility. In other words, anions normally only reach the outer surface and the large pores of an electrode, whereas the interior and small pores are difficult to use sufficiently, resulting in poor performance, especially at a high current density[41–43].

To further investigate the structural properties of the LSG/NMC composite, TEM and EDS mapping were carried out. Figure 4 shows the (a) TEM image, (b) selected area electron diffraction (SAED) pattern of the LSG, and (c) TEM image of LSG/NMC composite. As shown in Fig. 4a, the LSG appears to be stacked on another graphene layer and comprised three overlapping monolayers, which is consistent with Fig. 3c. It seems that the corrugated LSG with ripples and folded regions is exfoliated with an interlayer distance of ~0.36 nm (Supplementary Fig. S3a)[44]. A TEM SAED was measured to characterize the LSG, as shown in Fig. 4b. The intensity profile across a line (Fig. 4d-f) was taken from the three different regions. The intensity ratios of the LSG demonstrate that the intensity ratio ($I(1-210)/I(1-100)$) increases with an increasing number of graphene layers. The $I(1-210)/I(1-100)$ for the LSG is close to 1.55, corresponding to trilayer graphene (Fig. 4f). Figure 4c

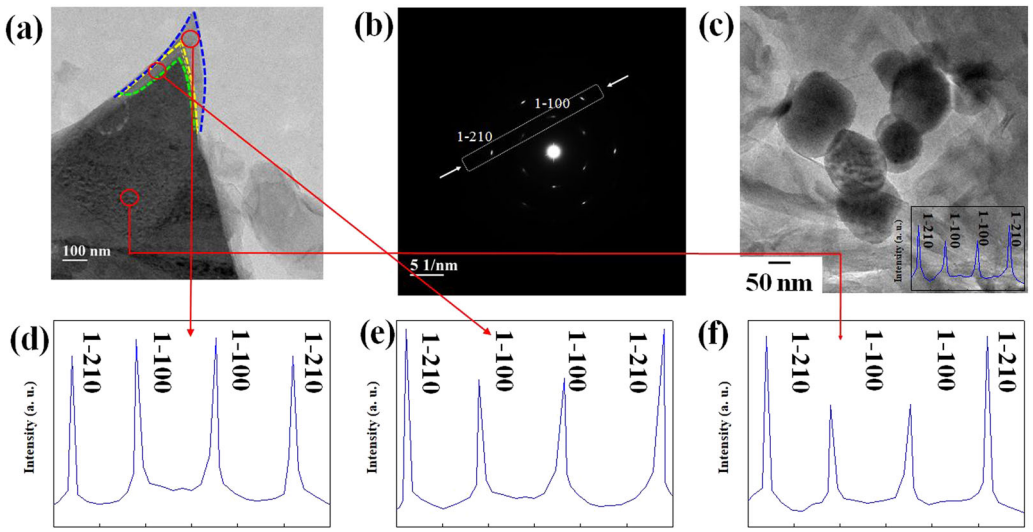


**Fig. 4 Morphological and structural characterization of the LSG and LSG/NMC composite. a** TEM images and **b** SAED pattern of the LSG, indicating that it comprised three layers. **c** TEM image of LSG/NMC composite (the inset shows the SAED pattern). Intensity profiles from the SAED patterns taken along the {1–210}, {1–100}, {1–100}, and {1–210} for the **d** single layer, **e** bilayer, and **f** trilayer LSG samples.

shows the distribution of NMC particles with sizes of 150–200 nm on the surface of the LSG. The composition of the NMC particles was confirmed to include Ni, Co, Mn, and O components by EDS in STEM mode (STEM-EDS), as shown in Supplementary Fig. S3b. The intensity ratio of the LSG/NMC is 1.32 (inset of Fig. 4c), which thus indicates that the LSG/NMC composite is a loosely stacked structure whereby the NMC is anchored onto the surface of the LSG, as shown in Fig. 3c[45]. The magnified HRTEM image (Supplementary Fig. S3c) clearly shows a lattice spacing of ~0.24 nm, which agrees well with the (003) lattice spacing of NMC[46]. In addition, the EDS results (Supplementary Fig. S3d) indicate the presence of Ni, Mn, and Co with an atomic ratio of ~1 : 1 : 1, which is the same as the designed value. Unlike the LSG, the morphology of the GO clearly contains typical flake-like shapes and is transparent, as shown in Supplementary Fig. S3e. The TEM image shows the disordered nature of the GO, and only diffraction rings and unresolved diffraction spots are observed in the SAED pattern (Supplementary Fig. S3f), clearly indicating that the GO is in an amorphous state[47].

The surface state and chemical composition of the LSG/NMC composite were obtained by high-resolution XPS. As indicated in Supplementary Fig. S4a, the binding energies at 855.1 and 872.3 eV are assigned to the Ni $2p_{3/2}$ and Ni $2p_{1/2}$ peaks, respectively. For the Co $2p$ bond, the high-resolution XPS spectrum could be resolved into Co $2p_{3/2}$ (779.8 eV) and Co $2p_{1/2}$ (795.3 eV) peaks (Supplementary Fig. S4b). The Mn $2p$ peaks at 642.8 and 654.3 eV can be assigned to the Mn $2p_{3/2}$ and Mn $2p_{1/2}$ peaks, respectively (Supplementary Fig. S4c). We can confirm that the dominant valences of Ni, Co, and Mn in the NMC are divalent, trivalent, and tetravalent, respectively. In addition, the single sharp C 1*s* peak (Supplementary Fig. S4d) appearing near 285 eV is assigned to C–C in the LSG/NMC composite. The positions of the binding-energy peaks are consistent with previous reports of NMC and LSG[48].

The average particle size of the H-HTO is ~0.8 μm (Supplementary Fig. S1c). The coating thickness is <10 nm (Supplementary Fig. S1d) and we can confirm that the $AlPO_4$ and carbon are uniformly coated on the entire surface of the HTO electrode through EDS element mapping of Al ($AlPO_4$) and C (carbon), as shown in Supplementary Fig. S1e.

Five LSG/NMC composites were prepared that had 1, 3, 5, 7, and 9 wt% NMC with respect to the LSG and the optimized concentration of NMC in LSG was investigated. Supplementary Fig. S5a shows the CV curves of the LSG/NMC composites with different NMC additions at a high scan rate of 50 mV/s. The rectangular and symmetric CV curves demonstrate ideal capacitive behavior. It can be clearly seen that the area surrounded by the CV curves for the LSG/NMC composites slightly increases as the amount of NMC in the composite increases, indicating a beneficial pseudocapacitive NMC reaction. However, the area decreased as the NMC content increased when the NMC content was more than 5 wt%. The initial charge and discharge curves (Supplementary Fig. S5b) are consistent with the results of the CV curves. An appropriate amount of NMC contributes to the capacity because of the synergistic effect of the LSG and NMC. The LSG/NMC composite reaches the maximum capacity value

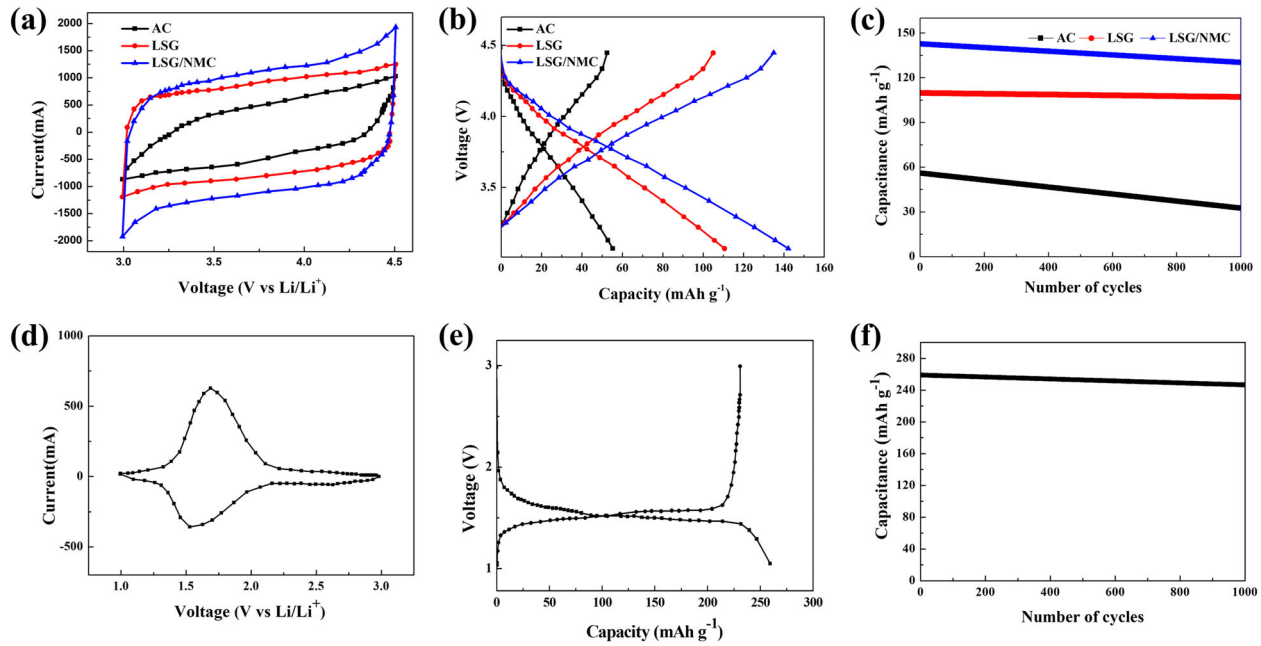


**Fig. 5 Electrochemical performance of the LSG/NMC, LSG, and AC cathodes, and H-HTO anode in a half-cell system. a** CV curves at a scan rate of 50 mV/s, **b** initial charge–discharge curves at a current density of 0.5 A/g, and **c** cycle performance of LSG/NMC, LSG, and AC cathodes at a current density of 0.5 A/g. **d** CV curves at a scan rate of 1 mV/s, **e** initial charge–discharge curves at a current density of 200 mA/g, and **f** cycle performance of H-HTO at a current density of 0.5 A/g. For the half-cell tests, cells were assembled into a two-electrode configuration with a Li metal counter electrode, a separator, and an electrolyte comprising 1.5 M lithium hexafluorophosphate in a 1:1 mixture of EC and DMC in a glove box.

(123.7 mAh/g) with the 5 wt% NMC addition and then it loses its capacity with a further increase in the NMC concentration. This is because excessive NMC leads to a high resistance due to a low conductivity[49,50]. These results indicate that the optimum amount of NMC added to the LSG is 5 wt%, and that excessive NMC has a negative effect on the electrochemical performance.

Before fabricating the hybrid supercapacitors, half-cell tests were performed to compare the electrochemical performance of the individual electrodes (LSG/NMC, LSG, and AC), as shown in Fig. 5. To demonstrate the advantages of the electrochemical performance of the LSG/NMC cathode for hybrid supercapacitors, we performed (a) CV, (b) galvanostatic charge–discharge, and (c) cycle measurements. The CV curves of LSG/NMC, LSG, and AC are shown in the potential range from 3.0 to 4.5 V at a scan rate of 50 mV/s. It is obvious that the CV curves from the LSG/NMC and LSG samples exhibit a nearly rectangular shape, indicating ideal electrical double-layer capacitive behavior. The increase in the current after the NMC loading into the LSG can be explained by the pseudocapacitive behavior of the NMC[51]. The area surrounded by the CV curve of the LSG/NMC composite significantly increases, which indicates an improved electrochemical behavior. This can be explained by the high ion-accessible surface area that originates from the high specific surface area and large pore size, ultimately leading to excellent electrochemical performance[51]. The CV curve of AC is distorted and has a narrow shape with an oblique angle, which is a result of the overpotential increase in the ion transport between the electrolyte and AC. This can also be explained by the large amount of micropores in the AC that do not contribute readily to adsorption/desorption under the same conditions[11,52]. Notably, the LSG/NMC composite retains its initial shape with no obvious distortion, even at a high scan rate of up to ~300 mV/s, as shown in Supplementary Fig. S6a (inset: an enlarged CV curve at a scan rate of 50 mV/s). This can be explained by the low contact resistance that results from the rapid interlayer charge transfer and unchanged capacitive behavior[52]. To obtain additional information about the potential of LSG/NMC composites as cathode materials for hybrid supercapacitors, galvanostatic charge–discharge measurements (Fig. 5b) were carried out. As expected, the LSG/NMC composite outperforms the LSG and AC in terms of its high initial capacity. The LSG/NMC composite shows a high initial discharge capacity of 127.3 mAh/g, which is higher than that of the LSG (98.2 mAh/g) and AC (49.5 mAh/g) at a current density of 0.5 A/g, suggesting that NMC plays a key role in achieving a high capacity. The decreased capacity of the AC can be explained by the carbon black, which has a small specific surface area. However, carbon black does not contribute to the capacity and, thus, the use of carbon

black degrades the performance as a function of its weight. Moreover, AC has a relatively high electrical resistance due to the limited diffusion of anions in the internal porous network. This is consistent with the results of the CV curves (Fig. 5a)[16]. The main reason for the poor capacity of the LSG is because ion accessibility is kinetically hindered in the stacked LSG. This implies that the highly conductive and unique structure of the LSG/NMC composite allows large numbers of ions to absorb onto the LSG surface and enables the pseudocapacitive behavior of the NMC, which contributes to more charge storage at the same current density than that for the other materials considered herein. The LSG tends to aggregate due to van der Waals interactions with adjacent layers. However, the NMC spacers between the LSG layers can play an important role in preventing the restacking of the LSG, resulting in additional electroactive sites for capacitive behavior[53].

It can also be inferred that the large number of micropores in AC limits ion adsorption/desorption on the surface of the electrode at a high current density. Moreover, LSG/NMC and LSG cathodes were prepared on aluminum foil directly without conductive additives and polymeric binding agents, which are commonly required not only to reinforce the adhesion between electrodes and substrates but also to increase the conductivity of the electrode. However, they have a negative effect on the electrochemical performance by increasing the resistivity and electrode weight (~20–30% of the total electrode weight)[54,55]. Thus, conductive additive and binder-free electrodes generally exhibit improved electrochemical performance. Importantly, the LSG/NMC composite not only has a high capacity but also achieves excellent retention (~98.1%) after 1000 cycles at a current density of 5.0 A/g, as shown in Fig. 5c. Although the poor conductivity of NMC increases the bulk solution resistance when the electrolyte, separator, and collector are included, a small amount of NMC is mainly inserted between the LSG layers and can minimize their stacking, thus facilitating easier ion and electron transfer to the electrode during the charge–discharge process, and thereby improving the rate capability and cycle performance[56]. Therefore, these results strongly suggest that the LSG/NMC cathode has a positive impact on the extraordinarily high electrochemical performance of hybrid supercapacitors.

Figure 5d shows that the CV curves of H-HTO have distinct pairs of redox peaks, resulting from the oxidation–reduction reactions of $Ti^{4+}$ ions in the potential range of 1.0–3.0 V at a scan rate of 1 mV/s. The potential separation between the anodic peaks ($E_a$) of ~1.68 V and cathodic peaks ($E_c$) of ~1.52 V originated from the oxidation–reduction process. There is a small gap (0.16 V) between the anodic and cathodic peaks, indicating a fast and reversible Li-ion intercalation into the H-HTO. This can be calculated by the following equation[11,57]:

**Table 2 Polarization values of the H-HTO anode at various scan rates from 1 to 20 mV/s.**

| | 1 mV/s | 2 mV/s | 5 mV/s | 10 mV/s | 20 mV/s |
|---|---|---|---|---|---|
| $E_a$ | 1.68 | 2.31 | 2.35 | 2.36 | 2.37 |
| $E_c$ | 1.52 | 1.90 | 1.89 | 1.88 | 1.87 |
| $\Delta E$ | 0.16 | 0.41 | 0.46 | 0.48 | 0.50 |

$$\Delta E = E_a - E_c \quad (2)$$

where $\Delta E$ is the difference between the anodic and cathodic peak potentials (polarizations), $E_a$ is the anodic peak, and $E_c$ is the cathodic peak. As shown in Supplementary Fig. S6b and Table 2, the polarizations slightly increase, but not significantly, with increasing scan rate due to diffusion-controlled ohmic contributions while maintaining their shape, suggesting that H-HTO is appropriate for highly efficient Li-ion transfer[58]. Therefore, polarization values are closely associated with the electrochemical performance. Figure 5e shows the initial charge–discharge profiles for the H-HTO with a plateau near 1.55 V (vs. $Li/Li^+$), which is the reversible redox potential of H-HTO. The H-HTO exhibited a capacity of 235 mAh/g at a current density of 200 mA/g, indicating that 8.6 Li ions could be inserted reversibly into the H-HTO anode for the first time[11]; its excellent reversibility of 86.1% retention after 20 cycles is also shown in Supplementary Fig. S6c. The capacity of H-HTO shows a remarkably long cycling stability (97.5% retention up to 1000 cycles) at a current density of 0.5 A/g, demonstrating its use as an effective and reliable anode material for hybrid supercapacitors (Fig. 5f). In addition, the H-HTO retains a high capacity of 170.8 mAh/g (72% of the initial capacity), even at a high current density of 5.0 A/g, as shown in Supplementary Fig. S6d. There are five advantages of H-HTO anodes for hybrid supercapacitors as follows: (i) there is a large amount of Li-ion insertion/extraction for a high capacity, (ii) there is a one-dimensional tunnel structure that enables fast access of Li ions (Supplementary Fig. S1f), (iii) there is a small volume change during the charge–discharge process, (iv) the novel hybrid coating allows for accelerated Li-ion diffusion and electron transport, and (v) it suppresses swelling[59]. These synergistic effects are expected to result in the excellent electrochemical performance of hybrid supercapacitors.

Based on the excellent electrochemical performances of the individual electrodes, we designed hybrid supercapacitors based on the LSG/NMC//H-HTO system

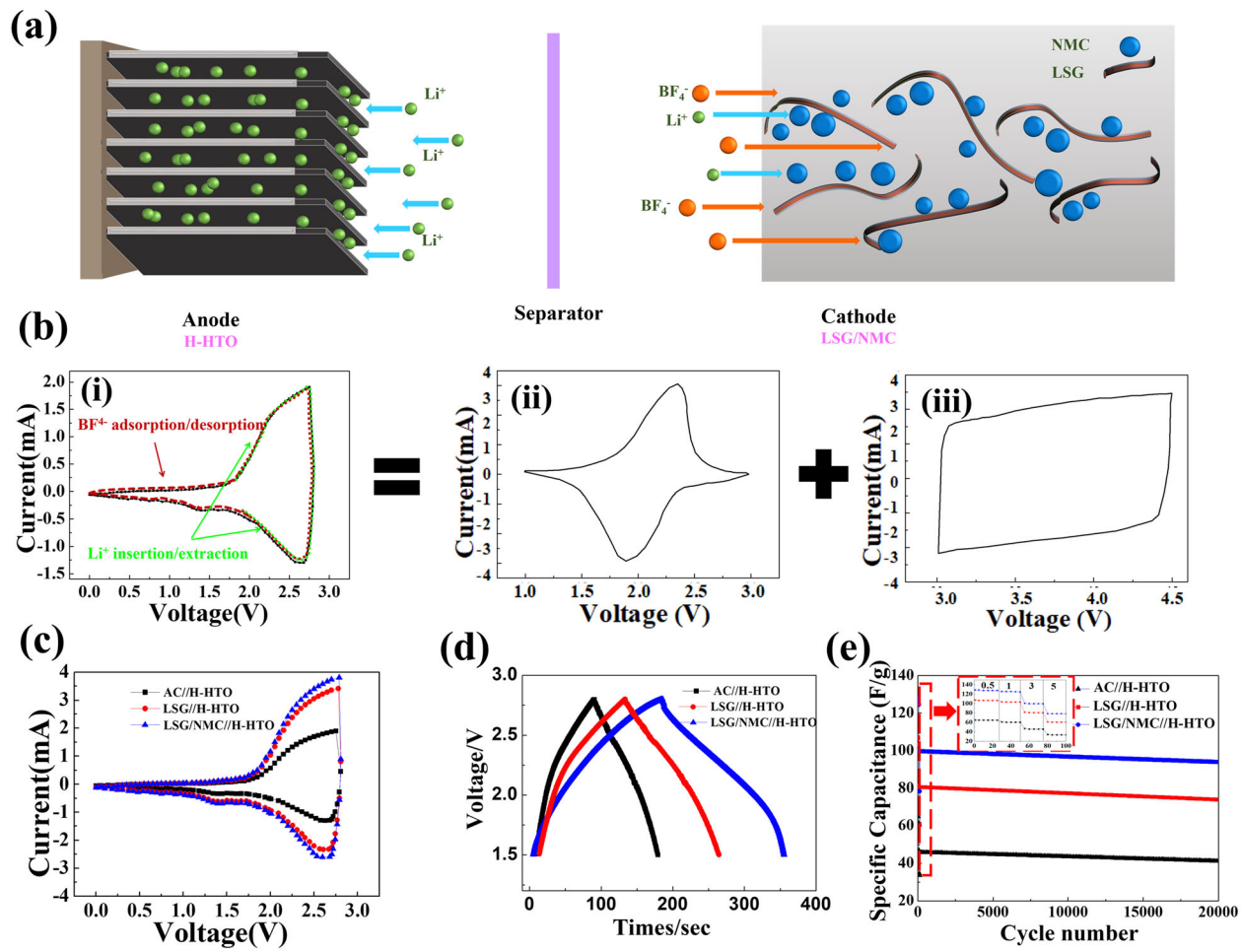


**Fig. 6 Concept and electrochemical performance of hybrid supercapacitors based on the LSG cathode and H-HTO anode in a full-cell system. a** Charging process of LSG/NMC//H-HTO hybrid supercapacitors. It is an optimized system with a highly accelerated Li-ion intercalating H-HTO anode and a non-faradaic AC cathode with an anion adsorption–desorption process. **b** CV curves of (i) the hybrid supercapacitor at voltages of 0–2.8 V, (ii) H-HTO anode at a voltage of 1.0–3.0 V, and (iii) LSG/NMC cathode at a voltage of 3.0–4.5 V. **c** CV curves at a scan rate of 0.1 V/s, **d** initial charge–discharge curves at a current density of 0.5 A/$g_{cathode+anode}$ and **e** long-term cycling performance of hybrid supercapacitors at a current density of 3.0 A/g (the inset shows the rate capability at various current rates from 0.5 A/g to 5 A/g).

(Fig. 6a) and investigated the electrochemical performance. Figure 6a shows that the electrochemical performance of the hybrid supercapacitors are derived from $PF_6^-$ ion adsorption/desorption at the cathode and Li-ion insertion/extraction at the anode[30,60].

Before manufacturing full-cell hybrid supercapacitors, the thicknesses of the anode and cathode were optimized by measuring the discharge retention according to the thickness variation (Supplementary Table S2). At a low current density of 0.1 A/g, the capacitance is proportional to the electrode thickness, as there is enough time for the electrochemical reaction at both electrodes. On the other hand, the capacitance retention decreases with increasing electrode thickness at a high current density of 3.0 A/g. This can be explained by the slow diffusion of Li ions from the anode at high charge/discharge rates[3]. Namely, the capacitance retention decreases proportionally as the current density increases. Only the upper region of the anode participates in the electrochemical reaction, whereas the lower region of the anode that does not participate in the reaction has a negative effect on the performance. Therefore, it is necessary to balance the thickness of both electrodes by removing unnecessary electrodes for high-performance hybrid supercapacitors. On the other hand, the capacitance retention of the cathode was increased in proportion to the electrode thickness. This is due to the adsorption–desorption of anions, which is a faster energy storage mechanism than that of lithium intercalation of the anode. Although the 90 μm anode and 300 μm cathode exhibit a high capacitance at a low current density, capacitance retention decreases quickly at high current densities. Considering the capacitance retention at various

thickness combinations, a 70 μm anode and 300 μm cathode were selected as the optimum thicknesses, because they provide the highest retention.

Unlike the ideal rectangular shape of supercapacitors, Fig. 6b shows that the CV curve of (i) hybrid supercapacitors has two different energy storage mechanisms, corresponding to the behavior of hybrid supercapacitors (hybrid behavior of supercapacitors and batteries)[61]. To understand this behavior, the CV curves of the (ii) Li intercalation redox electrode (H-HTO) and (iii) capacitive electrode (LSG/NMC) were measured. The H-HTO exhibits a pair of sharp peaks from the Faradaic reaction of H-HTO, whereas the LSG/NMC composite shows a nearly rectangular shape from a non-Faradaic reaction with an efficient interlayer charge transfer[62]. From the CV curves, it can be inferred that capacitive and redox reactions coexist in hybrid supercapacitors. The oxidation and reduction peaks in the hybrid supercapacitors are obtained through reversible electrochemistry of the $Ti^{4+}/Ti^{3+}$ redox couple in the H-HTO anode. Figure 6c shows the CV curves of the hybrid supercapacitors using LSG/NMC, LSG, and AC electrodes in the stable voltage window of 0–2.8 V due to a working voltage of 4.3 V for the cathode and 1.5 V for the anode at a scan rate of 0.1 V/s. All CV curves show the typical form found in hybrid supercapacitors, indicating that the curve has a pair of broad anodic peaks and cathodic peaks. Compared with those for LSG, the rectangular areas of the CV curves for the LSG/NMC composite are larger, implying that the introduction of NMC onto the LSG films not only increases the kinetics of $PF_6^-$ but also expands the number of active sites for electrochemical reactions. The small polarization between the anodic and cathodic peaks for the LSG/NMC composite is favorable for realizing both a high energy and power density (Table 3). The polarization of the LSG/NMC composite is sufficiently small (0.13 V), indicating that LSG/NMC composite delivers excellent reversibility during the charge–discharge process. The occurrence of these two peaks is mainly attributed to the slow Li-ion intercalation in the H-HTO. The main possible charge–discharge process of the hybrid supercapacitors can be expressed by the following reactions[31]:

$$\mathrm{LSG} + \mathrm{PF_6^-} \rightarrow \mathrm{LSG^+ \cdot PF_6^-} + e^- \ [\mathrm{Cathode}] \quad (3)$$

$$\mathrm{LiNi_{1/3}Co_{1/3}Mn_{1/3}O_2} \rightarrow \mathrm{Li_{1-x}Ni_{1/3}Co_{1/3}Mn_{1/3}O_2} + \mathrm{xLi^+} + \mathrm{xe^-} \ [\mathrm{Cathode}] \quad (4)$$

$$\mathrm{H_2Ti_{12}O_{25}} + \mathrm{xLi^+} + \mathrm{xe^-} \rightarrow \mathrm{Li_x \cdot H_2Ti_{12}O_{25}} \ [\mathrm{Anode}] \quad (5)$$

As is well known, CV curves can be divided into two parts as follows. (i) The first part is where the cathode only plays a role in charging below 1.5 V. It can be seen that both charge curves are nearly symmetric with respect to their corresponding discharge counterparts (namely, the so-called mirror effect), which is evident for their capacitive behaviors. However, the charge amount for the cathode is remarkably small. (ii) The second part is where the cathode and anode simultaneously contribute to charging beyond 1.5 V. However, the H-HTO plays a major role in charging the hybrid supercapacitors and the charge amount increases sharply. Supplementary Fig. S7a shows the CV curves of the hybrid supercapacitors using LSG/NMC//H-HTO for 100 cycles. After 100 cycles, the shape of the CV curve is almost identical to that of the first cycle with small polarization (Table 4), demonstrating that the rapid and reversible Li-ion kinetics of H-HTO match the quick $PF_6^-$ ion adsorption at the surface of the LSG/NMC.

**Table 3 Various parameters of hybrid supercapacitors based on the LSG/NMC//H-HTO, AC//H-HTO, LSG//H-HTO: IR drop, $R_{ct}$, and polarization values.**

| | AC//H-HTOZ | LSG//H-HTO | LSG/NMC//H-HTO |
|---|---|---|---|
| IR drop (Ω) | 0.26 | 0.20 | 0.11 |
| EIS first cycle | 0.047 | 0.036 | 0.030 |
| EIS after 1000 cycles | 0.06 | 0.047 | 0.039 |
| $E_a$ | 2.78 | 2.77 | 2.75 |
| $E_c$ | 2.59 | 2.60 | 2.62 |
| $\Delta E$ | 0.19 | 0.17 | 0.13 |

To assess the electrochemical performance of hybrid supercapacitors, the initial charge–discharge curves were measured at a current density of 0.5 A/g, as shown in Fig. 6d. All charge–discharge curves for the hybrid supercapacitors exhibit asymmetrical shapes, which is contrary to the shapes for supercapacitors. The discharge-specific capacitances of the hybrid supercapacitors can be calculated by the following equation[5]:

$$C = \frac{q}{\Delta V \times m} = \frac{\int i \Delta t}{\Delta V \times m} \quad (6)$$

where $C$ is the specific capacitance (F/g), $q$ is the total charge, $\Delta V$ is the potential range, $m$ is the mass of the active materials in hybrid supercapacitors, $i$ is the current, and $t$ is discharge time. The capacitance of the hybrid supercapacitors that use LSG/NMC, LSG, and AC cathodes are 141.5, 105.7, and 68.2 F/g, respectively. Notably, the LSG/NMC composite shows the highest capacitance herein, as the NMC acts as a spacer, ensuring that additional LSG regions can participate in electrochemical reactions, which is the key to achieving high-capacitance hybrid supercapacitors. In addition, the

**Table 4 Polarization values of the hybrid supercapacitors based on the LSG/NMC//H-HTO system for 100 cycles.**

| | 1 Cycle | 20 Cycles | 40 Cycles | 70 Cycles | 100 Cycles |
|---|---|---|---|---|---|
| $E_a$ | 2.75 | 2.76 | 2.77 | 2.78 | 2.79 |
| $E_c$ | 2.62 | 2.55 | 2.50 | 2.49 | 2.46 |
| $\Delta E$ | 0.13 | 0.21 | 0.27 | 0.29 | 0.33 |

capacitance of the LSG/NMC composite is still as high as 77.1 F/g (~55% retention), even at a high current density of 3.0 A/g, as shown in Supplementary Fig. S7b. The voltage drops (current–resistance (IR) drop) of the hybrid supercapacitors are due to the internal resistances of the hybrid supercapacitors, which is one of the most important factors for rate capability[63]. The IR drop was obtained using the following equation[3]:

$$R = \frac{V_{\text{charge}} - V_{\text{discharge}}}{2I} \quad (7)$$

where $V_{\text{charge}}$ is the voltage of the cell at the end charge, $V_{\text{discharge}}$ is the voltage of the cell at the starting discharge, and $I$ is the absolute value of charge and discharge current. The hybrid supercapacitors using LSG/NMC//HTO exhibited the lowest IR drop herein (Table 5) and exhibited a sufficiently small value (0.11 Ω at 0.5 A/g), indicating a very small value compared with that for previously reported hybrid supercapacitors[64,65]. This demonstrates the intrinsic reversibility even though the current density increased to 3.0 A/g[64].

The durable high rate capability and stable cycling of hybrid supercapacitors are two key parameters for their application in hybrid supercapacitors, and both are observed in Fig. 6e. The hybrid supercapacitors are first cycled at 0.5 A/g and then continuously cycled at 1.0, 3.0, and 5.0 A/g (inset of Fig. 6e). The cells were cycled at each rate for five cycles. When returning back to 3.0 A/g again after 20 cycles to assess the cycle performance, the capacity is fully recovered, indicating its excellent rate capability. In addition, the LSG/NMC composite shows excellent capacity retention up to 20,000 cycles with no obvious fading; the retention is as high as ~94.6% after 20,000 cycles at a current density of 3.0 A/g. These encouraging high-rate and ultra-long-life hybrid supercapacitors using LSG/NMC//H-HTO electrodes are supported by EIS measurements, as shown in Supplementary Fig. S7c, d. The EIS shows a small charge-transfer resistance ($R_{ct}$) for the hybrid supercapacitors, which is mainly attributed to the improved penetration of the Li ions and electrons into the hybrid coating and tunnel structure (Table 3). This indicates that H-HTO can provide good conductivity for hybrid supercapacitors. Most importantly, hybrid coatings are extremely effective

**Table 5 IR drop values of hybrid supercapacitors based on the LSG/NMC//H-HTO system at various current densities from 0.5 A/g to 3.0 A/g.**

| | 0.5 A/g | 1.0 A/g | 2.0 A/g | 3.0 A/g |
|---|---|---|---|---|
| IR drop (Ω) | 0.11 | 0.13 | 0.16 | 0.19 |

at inhibiting swelling during cycling, which can lead to an ultra-long cycle life and effectively prevent important safety issues[30]. Moreover, in terms of the cathode, the LSG/NMC composite shortens the ion diffusion length to provide fast ion kinetics and numerous active sites for charge storage. Consequently, we can conclude that pathways for smooth electron and ion transport are important for long-term cycling stability. One of the major concerns for hybrid supercapacitors during cycle tests is overheating, which in serious cases can cause thermal runaway due to the destruction of the solid electrolyte interface layer on the carbon-based electrode[66]. Supplementary Fig. S8a shows the surface temperature of the hybrid supercapacitors over 20,000 cycles. The surface temperature appears almost constant at ~26.5 °C during the cycle test, indicating that the LSG/NMC//H-HTO hybrid supercapacitors generate less heat. Thus, this system can meet ESD requirements of high stability and reliability. The rate capabilities of five LSG/NMC//H-HTO hybrid supercapacitors were assessed to determine their reproducibility, as shown in Supplementary Fig. S8b. There are no significant differences in the values of all samples. Therefore, it can be concluded that the improvement in the performance of the LSG/NMC//H-HTO hybrid supercapacitors is accompanied by good reproducibility.

Figure 7 shows the Ragone plots of the LSG/NMC//H-HTO hybrid supercapacitors to compare them with those of other previously reported hybrid supercapacitors. The power density ($P$) and energy density ($E$) were calculated as follows[61]:

$$P = \Delta V \times I/m \quad (8)$$

$$E = P \times t/3600 \quad (9)$$

$$\Delta V = (E_{\max} + E_{\min})/2 \quad (10)$$

where $E_{\max}$ and $E_{\min}$ are the potentials at the beginning of the discharge and at the end of the discharge ($V$), respectively; $I$ is the applied current ($A$); $t$ is the discharge time (seconds); and $m$ is the mass of active materials, including both the anode and cathode (g), in the hybrid supercapacitor. The hybrid supercapacitors using the LSG/NMC//H-HTO system deliver the highest energy density herein, while preserving their excellent power density. The energy density of the hybrid supercapacitors

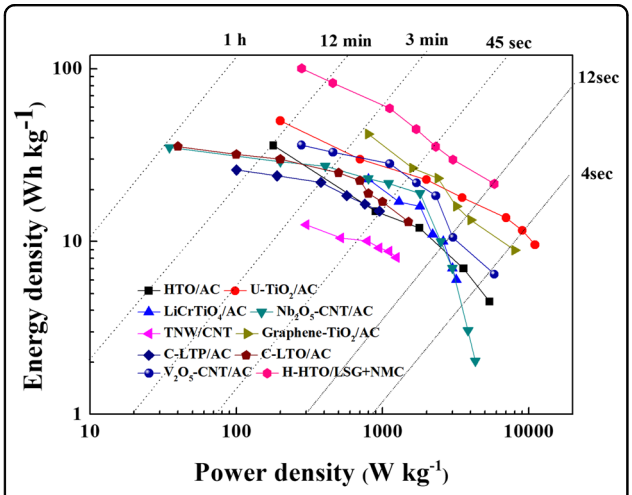


**Fig. 7 Energy and power densities of hybrid supercapacitors based on the LSG/NMC//H-HTO system compared with those from previously reported hybrid supercapacitors.** The LSG/NMC//H-HTO hybrid supercapacitors delivered significantly enhanced energy and power densities. The LSG/NMC//H-HTO hybrid supercapacitors are compared with other hybrid supercapacitors comprising $TiO_2$-(reduced graphene oxide)/AC, $TiO_2$-(B) nanowire (TNW)/carbon nanotube (CNT), C-$Li_4Ti_5O_{12}$ (LTO)/AC, C-$LiTi_2(PO_4)_3$ (LTP)/AC, $V_2O_5$-CNT/AC, $Nb_2O_5$-CNT/AC, $H_2T_{12}O_{25}$-AC, $LiCrTi_4$/AC, and urchin-like $TiO_2$/AC systems.

increases from 26.4 to 123.5 Wh/kg as the power density changes from 14074.8 to 208.2 W/kg, which still exceeds those of the $TiO_2$-(reduced graphene oxide)/AC[61], $TiO_2$-(B) nanowire/carbon nanotube (CNT)[7], C-$Li_4Ti_5O_{12}$ (LTO)/AC[67], C-$LiTi_2(PO_4)_3$/AC[68], $V_2O_5$-CNT/AC[69], $Nb_2O_5$-CNT/AC[70], $H_2T_{12}O_{25}$-AC[3], $LiCrTi_4$/AC[71], and urchin-like $TiO_2$/AC[72] systems. From these results, we can confirm that the hybrid supercapacitors comprising the LSG/NMC//H-HTO system exhibit the highest energy and power densities to date. The excellent performance can be ascribed to both the double-layer capacitive and pseudocapacitive behaviors at the LSG/NMC cathode and the preferable Li-ion intercalation kinetics at the H-HTO anode. It is also worth noting that the composition of the LSG/NMC//H-HTO system meets the stringent requirements for automotive applications, including hybrid EVs (HEVs) and plug-in HEVs[73,74].

## Conclusion

In summary, we propose a novel hybrid supercapacitor system based on an LSG/NMC cathode and an H-HTO anode. We demonstrated that hybrid supercapacitors have an outstanding energy density of 123.5 Wh/kg and power density of 14074.8 W/kg, but also an excellent cyclability of 94.6% after 20,000 cycles, which outperforms those of other hybrid supercapacitors. The reasons for this extraordinary electrochemical performance are mainly due to multiple synergy effects as follows: (i) the intrinsically excellent electrochemical performance of LSG; (ii) the anchoring of NMC spacers between the LSG layers, causing segregated graphene; (iii) the increase in the capacitance due to the additional effects of the NMC pseudocapacitive reaction; (iv) the combination of the tunnels and rapid pathways (hybrid coating) in the HTO anode to balance both electrodes; and (v) the suppression of gas formation via unwanted side reactions. These findings indicate that a hybrid supercapacitor using the LSG/NMC//H-HTO system could be a powerful and effective means for extraordinary performance. Moreover, the LSG/NMC composite, which does not require a binder and conductive additives, is expected to be advantageous for the miniaturization/weight reduction that are required for various portable devices and vehicle applications.

### Acknowledgements

This work was supported by "The development of battery capacitors using surface-modified LTO for 15C-rate fast charging and discharging ESS" at the Korea Institute of Energy Technology Evaluation and Planning (KETEP) and granted financial resources from the Ministry of Trade, Industry & Energy, Republic of Korea (No. 0172420108590), and by Basic Science Research Program through the National Research Foundation of Korea (NRF) funded by the Ministry of Education (2019R1A6A3A01097008).

### Author details

[1]Institute for Research in Electronics and Applied Physics, University of Maryland, College Park, MD 20742, USA. [2]Department of Advanced Materials Engineering, Daejeon University, Daejeon 34520, Republic of Korea. [3]R&D Center, Samwha Capacitor, Seoul, South Korea

### Author contributions

S.-H.L. and K.-Y.K. wrote the main manuscript. S.-H.L. and J.-R.Y. carried out the sample fabrication, measurements, and interpretation of the results. S.-H.L. and K.-Y.K. initiated the idea of working on the present topic. J.-R.Y. analyzed all experiments. S.-H.L. read and approved the final manuscript.

### Conflict of interest

The authors declare that they have no conflict of interest.

### Publisher's note

Springer Nature remains neutral with regard to jurisdictional claims in published maps and institutional affiliations.

**Supplementary information** is available for this paper at https://doi.org/10.1038/s41427-020-0204-0.

Received: 14 August 2019 Revised: 18 November 2019 Accepted: 26 November 2019.
Published online: 3 April 2020

### References

1. Simon, P., Gogotsi, Y. & Dunn, B. Where do batteries end and supercapacitors begin? *Science* **343**, 1210–1211 (2014).
2. Zhu, Y. et al. Carbon-based supercapacitors produced by activation of graphene. *Science* **332**, 1537–1541 (2011).
3. Lee, J. H. et al. Improved performance of cylindrical hybrid supercapacitor using activated carbon/niobium doped hydrogen titanate. *J. Power Sources* **301**, 348–354 (2016).
4. Wang, X. & Shen, G. Intercalation pseudo-capacitive $TiNb_2O_7$@carbon electrode for high-performance lithium ion hybrid electrochemical supercapacitors with ultrahigh energy density. *Nano Energy* **15**, 104 (2015).

5. Kim, J. H. & Lee, S. H. Use of carbon and $AlPO_4$ dual coating on $H_2Ti_{12}O_{25}$ anode for high stability hybrid supercapacitor. *J. Power Sources* **331**, 1–9 (2016).
6. Collins, J., Gourdin, G., Foster, M. & Qu, D. Carbon surface functionalities and SEI formation during Li intercalation. *Carbon* **92**, 193–244 (2015).
7. Xu, N. et al. The role of pre-lithiation in activated carbon/$Li_4Ti_5O_{12}$ asymmetric capacitors. *Electrochim. Acta* **236**, 443–450 (2017).
8. Naoi, K. 'Nanohybrid capacitor': the next generation electrochemical capacitors. *Fuel Cells* **10**, 825–833 (2010).
9. Chen, L. M., Lai, Q. Y., Hao, Y. J., Zhao, Y. & Ji, X. Y. Investigations on capacitive properties of the AC/$V_2O_5$ hybrid supercapacitor in various aqueous electrolytes. *J. Alloys Compd* **467**, 465–471 (2009).
10. Ke, Q., Zheng, M., Liu, H., Mao, L. & Wang, J. 3D $TiO_2$@$Ni(OH)_2$ core-shell arrays with tunable nanostructure for hybrid supercapacitor application. *Sci. Rep.* **5**, 1–11 (2015).
11. Zhang, L. L. & Zhao, X. S. Carbon-based materials as supercapacitor electrodes. *Chem. Soc. Rev.* **38**, 2520–2531 (2009).
12. Gao, H., Xiao, F., Ching, C. B. & Duan, H. High-performance asymmetric supercapacitor based on graphene hydrogel and nanostructured $MnO_2$. *ACS Appl. Mater. Interfaces* **4**, 2801–2810 (2012).
13. Naoi, K., Ishimoto, S., Miyamoto, J. & Naoi, W. Second generation 'nanohybrid supercapacitor': evolution of capacitive energy storage devices. *Energy Environ. Sci.* **5**, 9363–9373 (2012).
14. Stoller, M. D. & Ruoff, R. S. Best practice methods for determining an electrode material's performance for ultracapacitors. *Energy Environ. Sci.* **3**, 1294–1301 (2010).
15. Yi, R. et al. High-performance hybrid supercapacitor enabled by a high-rate Si-based anode. *Adv. Funct. Mater.* **24**, 7433–7439 (2014).
16. Cheng, Q. et al. Graphene and nanostructured $MnO_2$ composite electrodes for supercapacitors. *Carbon* **49**, 2917–2925 (2011).
17. He, Y. B. et al. Gassing in $Li_4Ti_5O_{12}$-based batteries and its remedy. *Sci. Rep.* **2**, 913 (2012).
18. Sheng, K., Sun, Y., Li, C., Yuan, W. & Shi, G. Ultrahigh-rate supercapacitors based on eletrochemically reduced graphene oxide for ac line-filtering. *Sci. Rep.* **2**, 247 (2012).
19. Peng, C., Zhang, S., Zhou, X. & Chen, G. Z. Unequalisation of electrode capacitances for enhanced energy capacity in asymmetrical supercapacitors. *Energy Environ. Sci.* **3**, 1499–1502 (2010).
20. Zhang, L. et al. Copper nanocrystal modified activated carbon for supercapacitors with enhanced volumetric energy and power density. *J. Power Sources* **236**, 215–223 (2013).
21. Anouti, M., Timperman, L., Mostafa el hilali, Boisset, A. & Galiano, H. Sulfonium bis(trifluorosulfonimide) plastic crystal ionic liquid as an electrolyte at elevated temperature for high-energy supercapacitors. *J. Phys. Chem. C* **116**, 9412–9418 (2012).
22. Liu, J. Charging graphene for energy. *Nat. Nanotechnol.* **9**, 739 (2014).
23. Shao, Y. et al. Graphene based electrochemical sensors and biosensors: a review. *Electroanalysis* **22**, 1027–1036 (2010).
24. Li, N. W. et al. Graphene@hierarchical meso-/microporous carbon for ultrahigh energy density lithium-ion capacitors. *Electrochim. Acta* **281**, 459–465 (2018).
25. Wu, Z. S. et al. Field emission of single-layer graphene films prepared by electrophoretic deposition. *Adv. Mater.* **21**, 1756–1760 (2009).
26. Huang, X., Zeng, Z., Fan, Z., Liu, J. & Zhang, H. Graphene-based electrodes. *Adv. Mater.* **24**, 5979–6004 (2012).
27. El-Kady, M. F., Strong, V., Dubin, S. & Kaner, R. B. Laser scribing of high-performance and flexible graphene-based electrochemical capacitors. *Science* **35**, 1326–1330 (2012).
28. Peng, Z., Lin, J., Ye, R., Samuel, E. L. G. & Tour, J. M. Flexible and stackable laser-induced graphene supercapacitors. *ACS Appl. Mater. Interfaces* **7**, 344–3419 (2015).
29. Wu, Z. S. et al. Graphene/metal oxide composite electrode materials for energy storage. *Nano Energy* **1**, 107–131 (2012).
30. Wu, Z. S. et al. Graphene anchored with $Co_3O_4$ nanoparticles as anode of lithium ion batteries with enhanced reversible capacity and cyclic performance. *ACS Nano* **4**, 3187–3194 (2010).
31. Wu, Z. S. et al. Anchoring hydrous $RuO_2$ on graphene sheets for high-performance electrochemical capacitors. *Adv. Funct. Mater.* **20**, 3595–3602 (2010).
32. Shaju, K. M., Subba Rao, G. V. & Chowdari, B. V. R. Performance of layered $Li(Ni_{1/3}Co_{1/3}Mn_{1/3})O_2$ as cathode for Li-ion batteries. *Electrochim. Acta* **48**, 145–151 (2002).
33. Liu, S. et al. Enhancing electrochemical performance of $LiNi_{0.6}Co_{0.2}Mn_{0.2}O_2$ by lithium-ion conductor surface modification. *Electrochim. Acta* **224**, 171–177 (2017).
34. Hao, Y. et al. Probing layer number and stacking order of few-layer graphene by Raman spectroscopy. *Small* **6**, 195–200 (2010).
35. Kang, Y. et al. Incorporate boron and nitrogen into graphene to make BCN hybrid nanosheets with enhanced microwave absorbing properties. *Carbon* **61**, 200–208 (2013).
36. Tian, H. et al. Wafer-scale integration of graphene-based electronic, optoelectronic and electroacoustic devices. *Sci. Rep.* **4**, 3598 (2014).
37. Zeng, J. J. & Lin, Y. J. Hybrid diodes based on n-type Ge and conductive polymer doped by graphene oxide sheets with and without reduction treatment. *J. Appl. Phys.* **113**, 1–5 (2013).
38. Liu, X., Li, H., Li, D., Ishida, M. & Zhou, H. PEDOT modified $LiNi_{1/3}Co_{1/3}Mn_{1/3}O_2$ with enhanced electrochemical performance for lithium ion batteries. *J. Power Sources* **243**, 374–380 (2013).
39. Tu, Z. et al. Controllable growth of 1–7 layers of graphene by chemical vapour deposition. *Carbon* **73**, 252–258 (2014).
40. Lee, S. H., Lee, K. H. & Zhong, Z. Wafer scale homogeneous bilayer graphene films by chemical vapor deposition. *Nano Lett.* **10**, 4702–4707 (2010).
41. Xu, X. et al. Facile synthesis of novel graphene sponge for high performance capacitive deionization. *Sci. Rep.* **5**, 8458 (2015).
42. Wimalasiri, Y. & Zou, L. Carbon nanotube/graphene composite for enhanced capacitive deionization performance. *Carbon* **59**, 464–471 (2013).
43. Liu, Y. et al. Porous carbon spheres via microwave-assisted synthesis for capacitive deionization. *Electrochim. Acta* **151**, 489–496 (2015).
44. Akhavan, O., Kalaee, M., Alavi, Z. S., Ghiasi, S. M. A. & Esfandiar, A. Increasing the antioxidant activity of green tea polyphenols in the presence of iron for the reduction of graphene oxide. *Carbon* **50**, 3015–3025 (2012).
45. Salvatierra, R. V., Domingues, S. H., Oliveira, M. M. & Zarbin, A. J. G. Tri-layer graphene films produced by mechanochemical exfoliation of graphite. *Carbon* **57**, 410–415 (2013).
46. Xiong, W., Jiang, Y., Yang, Z., Li, D. & Huang, Y. High-performance hierarchical $LiNi_{1/3}Mn_{1/3}Co_{1/3}O_2$ microspheres synthesized via a facile template-sacrificial route. *J. Alloys Compd* **589**, 615–621 (2014).
47. Krishnamoorthy, K., Veerapandian, M., Yun, K. & Kim, S. J. The chemical and structural analysis of graphene oxide with different degrees of oxidation. *Carbon* **54**, 38–49 (2013).
48. Venkateswara Rao, C., Leela Mohana Reddy, A., Ishikawa, Y. & Ajayan, P. M. $LiNi_{1/3}Co_{1/3}Mn_{1/3}O_2$–graphene composite as a promising cathode for Lithium-ion batteries. *ACS Appl. Mater. Interfaces* **3**, 2966–2972 (2011).
49. Deng, S. et al. Synthesis and electrochemical properties of MnO2 nanorods/graphene composites for supercapacitor applications. *Electrochim. Acta* **111**, 707–712 (2013).
50. Li, Z., Wang, J., Liu, S., Liu, X. & Yang, S. Synthesis of hydrothermally reduced graphene/MnO2 composites and their electrochemical properties as supercapacitors. *J. Power Sources* **196**, 8160–8165 (2011).
51. Hwang, J. Y. et al. Direct preparation and processing of graphene/$RuO_2$ nanocomposite electrodes for high-performance capacitive energy storage. *Nano Energy* **18**, 57–70 (2015).
52. Zhou, Q., Gao, J., Li, C., Chen, J. & Shi, G. Composite organogels of graphene and activated carbon for electrochemical capacitors. *J. Mater. Chem. A* **1**, 9196–9201 (2013).
53. Wu, C. et al. Three-dimensional $Co_3O_4$/flocculent graphene hybrid on Ni foam for supercapacitor applications. *J. Mater. Chem. A* **2**, 15987–15994 (2014).
54. Zhang, J., Zhao, X., Huang, Z., Xu, T. & Zhang, Q. High-performance all-solid-state flexible supercapacitors based on manganese dioxide/carbon fibers. *Carbon* **107**, 844–851 (2016).
55. Wu, Z. S. et al. Three-dimensional nitrogen and boron Co-doped graphene for high-performance all-solid-state supercapacitors. *Adv. Mater.* **24**, 5130–5135 (2012).
56. Chen, Y. et al. Enhanced electrochemical performance of laser scribed graphene films decorated with manganese dioxide nanoparticles. *J. Mater. Sci: Mater. Electron* **27**, 2564–2573 (2016).
57. Lee, S. H. & Im, I. H. Excellent performance hybrid supercapacitors based on $LiNi_{1/3}Mn_{1/3}Co_{1/3}O_2$/activated carbon electrode. *Mater. Lett.* **231**, 38–42 (2018).
58. Yu, X., Lu, B. & Xu, Z. Super long-life supercapacitors based on the construction of nanohoneycomb-like strongly coupled $CoMoO_4$–3D graphene hybrid electrodes. *Adv. Mat.* **26**, 1044–1051 (2014).

59. Akimoto, J., Kijima, N., Hayakawa, H., Takahashi, Y., & Idemoto, Y. Titanium oxide, method for manufacturing the same, and lithium secondary battery using the same as active material, US Patent No. 8,309,253 (2012).
60. Hsieh, C. T., Lin, J. Y. & Mo, C. Y. Improved storage capacity and rate capability of $Fe_3O_4$–graphene anodes for lithium-ion batteries. *Electrochim. Acta* **58**, 119–124 (2011).
61. Kim, H. et al. A novel high-energy hybrid supercapacitor with an anatase $TiO_2$–reduced graphene oxide anode and an activated carbon cathode. *Adv. Energy Mater.* **3**, 1500–1506 (2013).
62. Peng, L. et al. Ultrathin two-dimensional $MnO_2$/graphene hybrid nanostructures for high-performance, flexible planar supercapacitors. *Nano Lett.* **13**, 2151–215 (2013).
63. Sum, G. et al. Hybrid fibers made of molybdenum disulfide, reduced graphene oxide, and multi-walled carbon nanotubes for solid-state, flexible, asymmetric supercapacitors. *Angew. Chem. Int. Ed.* **54**, 4651 (2015).
64. Chou, T. C., Doong, R. A., Hu, C. C., Zhang, B. & Su, D. S. Hierarchically porous carbon with manganese oxides as highly efficient electrode for asymmetric supercapacitors. *ChemSusChem* **7**, 841–847 (2014).
65. Choi, H. J., Lee, S. H., Kim, J. H., Kim, H. K. & Kim, J. M. Zinc doped $H_2Ti_{12}O_{25}$ anode and activated carbon cathode for hybrid supercapacitor with superior performance. *Electrochim. Acta* **251**, 613–620 (2017).
66. Amine, K. et al. Nanostructured anode material for high-power battery system in electric vehicles. *Adv. Mater.* **22**, 3052–3057 (2010).
67. Jung, H. G., Venugopal, N., Scrosati, B. & Sun, Y. K. A high energy and power density hybrid supercapacitor based on an advanced carbon-coated $Li_4Ti_5O_{12}$ electrode. *J. Power Sources* **221**, 266–271 (2013).
68. Aravindan, V. et al. Carbon coated nano-$LiTi_2(PO_4)_3$ electrodes for non-aqueous hybrid supercapacitors. *Phys. Chem. Chem. Phys.* **14**, 5808–5814 (2012).
69. Aravindan, V. et al. Fabrication of high energy-density hybrid supercapacitors using electrospun $V_2O_5$ nanofibers with a self-supported carbon nanotube network. *ChemPlusChem* **77**, 570–575 (2012).
70. Wang, X. et al. High-performance supercapacitors based on nanocomposites of $Nb_2O_5$ nanocrystals and carbon nanotubes. *Adv. Energy Mater.* **1**, 1089–1093 (2011).
71. Aravindan, V., Chuiling, W. & Madhavi, S. High power lithium-ion hybrid electrochemical capacitors using spinel $LiCrTiO_4$ as insertion electrode. *J. Mater. Chem.* **22**, 16026–16031 (2012).
72. Choi, H. J., Kim, J. H., Kim, H. K., Lee, S. H. & Lee, Y. H. Improving the electrochemical performance of hybrid supercapacitor using well-organized urchin-like $TiO_2$ and activated carbon. *Electrochim. Acta* **208**, 202–210 (2016).
73. Wachsman, E. D., Marlowe, C. A. & Lee, K. T. Role of solid oxide fuel cells in a balanced energy strategy. *Energy Environ. Sci.* **5**, 5498–5509 (2012).
74. Seok, J. W., Lee, J., Rodgers, T., Ko, D. H. & Shim, J. H. Effect of $LiPO_2F_2$ electrolyte additive on surface electrical properties of $LiNi_{0.6}Co_{0.2}Mn_{0.2}O_2$ cathode. *Trans. Electr. Electron. Mater.* **20**, 548–553 (2019).